RESEARCH ARTICLE

Key Points:
- Region 2 field-aligned currents drive additional ionospheric O^+ outflow
- This additional outflow feeds the ring current, creating a feedback system
- Ionospheric outflow is a tightly coupled piece of the M-I system

Correspondence to:
D. T. Welling,
dwelling@umich.edu

The two-way relationship between ionospheric outflow and the ring current

D. T. Welling[1], V. K. Jordanova[2], A. Glocer[3], G. Toth[1], M. W. Liemohn[1], and D. R. Weimer[4]

[1]Department of Atmospheric, Oceanic, and Space Sciences, University of Michigan, Ann Arbor, Michigan, USA, [2]Los Alamos National Laboratory, Los Alamos, New Mexico, USA, [3]NASA Goddard Space Flight Center, Greenbelt, Maryland, USA, [4]Center for Space Science and Engineering Research, Bradley Department of Electrical and Computer Engineering, Virginia Polytechnic Institute and State University, Blacksburg, Virginia, USA

Abstract It is now well established that the ionosphere, because it acts as a significant source of plasma, plays a critical role in ring current dynamics. However, because the ring current deposits energy into the ionosphere, the inverse may also be true: the ring current can play a critical role in the dynamics of ionospheric outflow. This study uses a set of coupled, first-principles-based numerical models to test the dependence of ionospheric outflow on ring current-driven region 2 field-aligned currents (FACs). A moderate magnetospheric storm event is modeled with the Space Weather Modeling Framework using a global MHD code (Block Adaptive Tree Solar wind Roe-type Upwind Scheme, BATS-R-US), a polar wind model (Polar Wind Outflow Model), and a bounce-averaged kinetic ring current model (ring current atmosphere interaction model with self-consistent magnetic field, RAM-SCB). Initially, each code is two-way coupled to all others except for RAM-SCB, which receives inputs from the other models but is not allowed to feed back pressure into the MHD model. The simulation is repeated with pressure coupling activated, which drives strong pressure gradients and region 2 FACs in BATS-R-US. It is found that the region 2 FACs increase heavy ion outflow by up to 6 times over the noncoupled results. The additional outflow further energizes the ring current, establishing an ionosphere-magnetosphere mass feedback loop. This study further demonstrates that ionospheric outflow is not merely a plasma source for the magnetosphere but an integral part in the nonlinear ionosphere-magnetosphere-ring current system.

1. Introduction

It is well established that the ionosphere acts as an important source of plasma to the magnetosphere. Ionospheric H^+, He^+, and O^+ are first accelerated into the magnetosphere via a number of mechanisms. Pressure gradients and ambipolar electric fields form the so-called "classical polar wind" [*Axford*, 1968; *Banks and Holzer*, 1968; *Ganguli*, 1996]. Additional effects, such as wave-particle transverse heating [e.g., *Chaston et al.*, 2004, 2007], centrifugal acceleration [e.g., *Cladis*, 1986; *Horwitz et al.*, 1994], and effects of hot electron populations [e.g., *Barakat and Schunk*, 1983; *Barakat et al.*, 1998; *Khazanov et al.*, 1997], drive additional acceleration, sometimes referred to as "nonclassical" or "generalized" polar wind. The outflowing material populates the lobes and plasma sheet, eventually reaching the inner magnetosphere during periods of forward convection [e.g., *Chappell et al.*, 1987; *Delcourt et al.*, 1993; *Moore and Delcourt*, 1995; *Chappell et al.*, 2000; *Huddleston et al.*, 2005; *Moore*, 2005; *Welling and Ridley*, 2010a].

A clear link between solar drivers and the amount of outflowing ionospheric particles has been established both in observations and in numerical models. Observed outflow fluences have been shown to correlate strongly with the activity index, Kp [*Yau et al.*, 1988; *Elliott et al.*, 2001], solar wind electric field and interplanetary magnetic field (IMF) magnitude [*Cully et al.*, 2003], IMF B_Z polarity [*Lennartsson et al.*, 2004], and upstream dynamic pressure [e.g., *Moore et al.*, 1999; *Elliott et al.*, 2001; *Cully et al.*, 2003; *Lennartsson et al.*, 2004]. These dynamics have clearly manifested in global models using simple inner boundary conditions as a proxy for outflowing plasma [*Winglee*, 1998; 2000; *Siscoe et al.*, 2001; *Walker et al.*, 2003; *Zhang et al.*, 2007; *Welling and Liemohn*, 2014]. From such results, it can be understood that outflow dynamics are beholden to solar dynamics.

The importance of ionospheric outflow on ring current development is also well established. During periods of strong solar driving, O^+ of ionospheric origin drastically increases in the plasma sheet and geosynchronous locations [e.g., *Young et al.*, 1982; *Lennartsson and Shelley*, 1986; *Nosé et al.*, 2003; *Nosé*, 2005; *Denton et al.*,

2005] and the inner magnetosphere [*Sharp et al.*, 1985; *Hamilton et al.*, 1988; *Daglis et al.*, 1999; *Kozyra*, 2002; *Kronberg et al.*, 2012]. Ring current modelers have switched from using basic empirical models of plasma sheet composition [e.g., *Fok et al.*, 1995; *Jordanova et al.*, 1996; *Kozyra et al.*, 1998; *Liemohn et al.*, 1999; *Ebihara and Ejiri*, 2000; *Jordanova et al.*, 2006] to dynamic, physics-based models that capture the evolution from outflow to plasma sheet [*Moore*, 2005; *Moore et al.*, 2007; *Fok et al.*, 2011; *Welling et al.*, 2011; *Ilie et al.*, 2013]. It has been found that spatial and temporal dynamics of the ionospheric source are important in controlling ring current development and are distinct from the solar source. Because of this, the ring current can be considered to be dependent on ionospheric outflow.

An interesting scenario emerges when the inverse is considered: what role does the ring current play in the development of ionospheric outflows? The ring current also deposits energy into the ionosphere via direct particle precipitation [e.g., *Galand and Richmond*, 2001; *Fang et al.*, 2007a, 2007b, 2007c], precipitation caused by ring current-driven waves [e.g., *Frey*, 2004; *Sandanger et al.*, 2007; *Jordanova et al.*, 2008; *Søraas et al.*, 2013], and generation of region 2 field-aligned currents (R2 FACs) [e.g., *Wolf*, 1983; *Liemohn et al.*, 2001; *Anderson et al.*, 2005; *Zheng et al.*, 2006; *Buzulukova et al.*, 2010]. Could ring current input play a role in driving ionospheric outflow that rivals that of the solar wind? If so, the potential for a nonlinear feedback system between the two domains becomes very real. Recent studies have begun to establish such feedback mechanisms between magnetospheric tail dynamics and ionospheric outflow [*Brambles et al.*, 2011; *Ouellette et al.*, 2013; *Brambles et al.*, 2013; *Moore et al.*, 2014]; could the ring current be involved in a similar relationship?

This study uses coupled, first-principles-based numerical models to assess the two-way relationship between ionospheric outflow and the ring current. A magnetospheric storm is modeled using a global magnetohydrodynamic (MHD) code, an ionospheric outflow model, and a ring current model, all coupled together. Initially, the ring current model is not allowed to feed back into the system: it only takes inputs from the other models but does not return any values. To "switch on" ring current feedback, pressure from the ring current model is used to create more accurate pressure gradients in the global model, driving clear region 2 field-aligned currents (FACs) through the system. FACs are important in controlling the ambipolar electric field at sub-MHD altitudes [e.g., *Gombosi and Nagy*, 1989, discussed in detail in section 3.2]. The effect of closing the ionosphere-magnetosphere-ring current loop on heavy ion outflow and, in turn, ring current development is investigated.

2. Methodology

Four coupled codes are used to simulate outflow, ionospheric electrodynamics, global magnetospheric dynamics, and the ring current: the Polar Wind Outflow Model (PWOM), the Ridley Ionosphere Model (RIM), the Block Adaptive Tree Solar wind Roe-type Upwind Scheme (BATS-R-US) MHD model, and the ring current atmosphere interaction model with self-consistent magnetic field (RAM-SCB). These codes are executed, synchronized, and coupled through the Space Weather Modeling Framework (SWMF) [*Tóth et al.*, 2005, 2012], a flexible tool for performing complex simulations of the multiscale space environment. These models and their configurations match that of *Welling et al.* [2011], so only brief descriptions are repeated here. The only exception is the recently developed two-way coupling between RAM-SCB and BATS-R-US, for which further detail is provided. The relationship between these models is summarized in Figure 1.

BATS-R-US MHD [*Powell et al.*, 1999; *De Zeeuw et al.*, 2000] is used to simulate the global magnetospheric dynamics. This code has a rich history of terrestrial applications [*Gombosi et al.*, 1998; *Ridley et al.*, 2002; *Tóth et al.*, 2007; *Zhang et al.*, 2007]. The only external input to BATS-R-US is the upstream solar wind and interplanetary magnetic field (IMF) conditions. In the simulations here, BATS-R-US' highly configurable grid is set to use approximately 1.9 million grid cells. About the inner boundary, a sphere of radius 2.5 Earth radii (R_E), the resolution is the finest with a spacing of $1/8R_E$. Nearly all areas of interest, including the inner magnetosphere, lobes, and central plasma sheet, lie in regions whose resolution is $1/4R_E$.

In this study, the multispecies MHD equations, described by *Ma et al.* [2002] and *Welling and Ridley* [2010a], are solved, allowing for densities of three separate species (H^+, He^+, and O^+) to be tracked [*Glocer et al.*, 2009a]. This equation set includes independent continuity equations for each species, but only a single energy and momentum equation equation, making it effectively a single fluid. While a true multifluid approach would yield a more descriptive solution, multispecies yields qualitatively similar results to a true multifluid approach [*Glocer et al.*, 2009b].
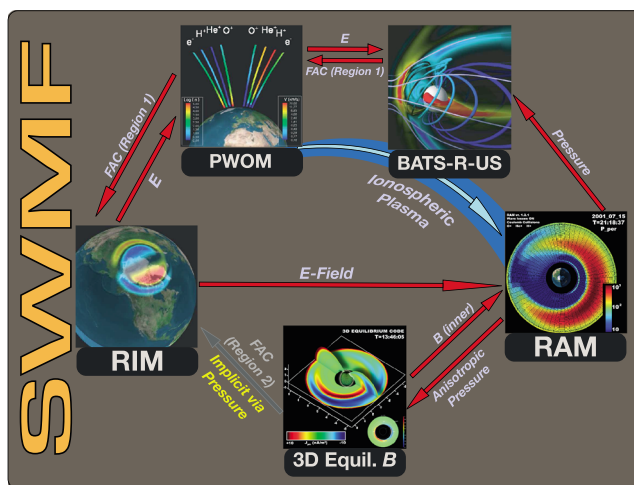
Figure 1. A diagram summarizing the coupling between the models used in this study. All couplings take place through the Space Weather Modeling Framework. Red arrows denote couplings that are used in this study; gray arrows denote couplings that are either implicitly achieved or disabled. The large blue arrow represents the travel of ionospheric outflow from the ionosphere through the magnetosphere and to the ring current.

For planetary magnetosphere use, BATS-R-US is nearly always coupled to a height-integrated ionospheric electrodynamics solver [*Ridley and Liemohn*, 2002; *Ridley et al.*, 2004]. This model receives FACs from BATS-R-US and uses them, along with an empirically based conductance pattern, to calculate the electric potential. Values are solved over the whole globe at every 2° in longitude and 1° latitude. The potential values are then used to set the tangential velocity about the MHD inner boundary. An important input to this model is the $F_{10.7}$ radio flux, a proxy for solar extreme ultraviolet irradiance, which scales the conductance.

PWOM [*Glocer et al.*, 2007, 2009a] is used to model ion dynamics throughout the "gap region," or the region between the upper boundary of most ionospheric electrodynamic models (i.e., 1000 km) and the inner boundary of most MHD models ($2 – 3$ R_E or $\sim 6000 – 13000$ km). The PWOM solves the gyrotropic transport equations of O^+, He^+, H^+, and electrons along many noninteracting, one-dimensional, radial flux tubes. In this study, 128 flux tubes are used. Horizontal motion is obtained by allowing each flux tube to advect with the local $E \times B$ velocity as obtained from the ionospheric electrodynamics model. Additionally, the PWOM receives FAC information from BATS-R-US, which is used to set the electron velocity along each flux tube via conservation of current density given the ion velocity. Electron velocity factors into the electron energy equation [*Glocer et al.*, 2007], driving adiabatic changes in electron temperature [*Gombosi and Nagy*, 1989]. Further, both electron temperature and velocity play dominant roles in the ambipolar electric field calculation, making the FAC input critical for determining ion outflow values. In more recent versions of PWOM, FACs also act as a proxy for topside electron heat flux [*Welling et al.*, 2011]. The resulting radial velocity and density for each ion species are used to set the inner boundary conditions in BATS-R-US, effectively driving ionospheric outflow in the MHD model.

Finally, the ring current is simulated using RAM-SCB. This model combines a bounce-averaged kinetic drift model of ring current ions [*Jordanova et al.*, 1996, 1997, 2006, 2010a] with a force balance model of the magnetic field [*Zaharia et al.*, 2004, 2005, 2006, *Zaharia*, 2008; *Zaharia et al.*, 2010], yielding magnetically self-consistent drift physics. In this study, almost all inputs to RAM-SCB are obtained from the other models. Density, temperature, and composition are obtained from BATS-R-US and are used to set the outer boundary flux by assuming a Maxwellian. Electric field from the ionospheric electrodynamics model is mapped along magnetic field lines to the equatorial plane. Magnetic field is a required outer boundary condition and initial condition to the self-consistent field calculation. The SCB submodel represents the field as a set of Euler potential shells. Constructing these shells in a manner that keeps pace with the other coupled codes is difficult and prone to geometrical errors. As such, magnetic field boundary for the SCB submodel is provided via the empirical model of *Tsyganenko* [1989] using the observed *Kp* index. The SCB submodel distorts this field to maintain magnetic self-consistency with the modeled anisotropic pressure distribution calculated by the RAM submodel. While this approach breaks magnetic consistency with the MHD model, the expected
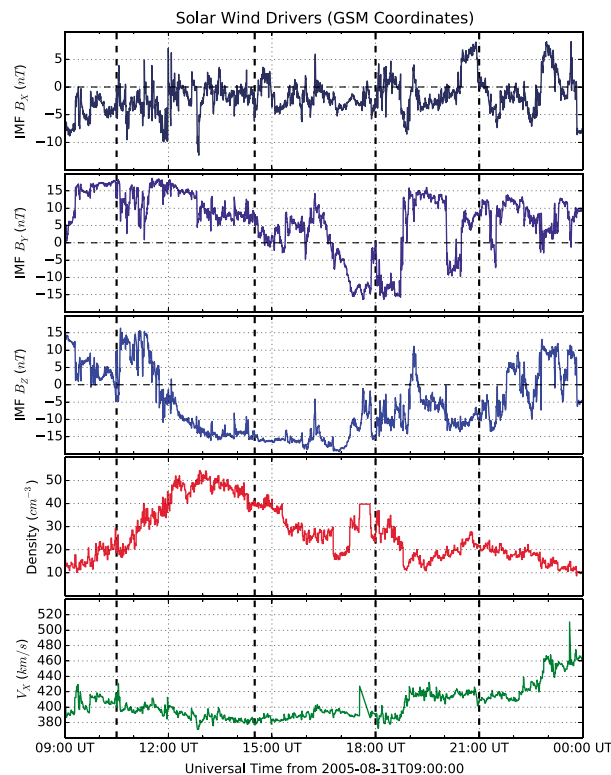
Figure 2. Solar wind conditions used to drive the simulations in this study. Interplanetary (first panel) B_X, (second panel) B_Y, and (third panel) B_Z are shown, respectively, followed by (fourth panel) solar wind number density and (fifth panel) earthward velocity. The vertical dashed lines mark epochs of interest used throughout the study.

difference is likely small and should not affect the results of this study in a significant manner.

In this study, RAM-SCB is allowed to return plasma pressure to BATS-R-US, two-way coupling the models. Following previous approaches [*De Zeeuw et al.*, 2004; 2004; *Glocer et al.*, 2013], pressure in the MHD model is "nudged" toward the RAM-SCB solution via the expression

$$p'_{GM} = p_{GM} + \min\left(1, \frac{dt}{\tau_{couple}}\right)(p_{IM} - p_{GM})$$

(1)

where p is plasma pressure, the subscripts GM and IM indicate the global magnetosphere (BATS-R-US) and inner magnetosphere (RAM-SCB) models, respectively, the prime superscript indicates pressure after the coupling, and τ_{couple} is a time constant introduced to maintain solution stability. Using this scheme, p_{GM} and p_{IM} converge after a time of $2\tau_{couple}$. When pressure coupling is activated in this study, a τ_{couple} of 60 s is used. In similar studies that leverage such pressure coupling, the results have been larger pressure and pressure gradient values in the MHD results which, in turn, drive stronger region 2 FACs [*De Zeeuw et al.*, 2004; *Pembroke et al.*, 2012; *Glocer et al.*, 2013].

These models all have a thorough history of data-model validation that demonstrates their ability to reproduce key observed features of the magnetosphere-ionosphere system. BATS-R-US and its associated ionosphere electrodynamics model have repeatedly shown high aptitude for reproducing observed magnetic field about the inner and outer magnetosphere [*Welling and Ridley*, 2010b; *Rastätter et al.*, 2011], field-aligned current patterns [*Ridley et al.*, 2002; *Korth et al.*, 2011], and the resulting ground-based perturbations [*Yu and Ridley*, 2008; *Pulkkinen et al.*, 2013]. The PWOM has demonstrated the ability to reproduce quiet time density and temperature altitude profiles [*Glocer et al.*, 2012]. Using PWOM to drive outflow into BATS-R-US has given the latter the ability to reproduce in situ observations of H^+ and O^+ densities [*Glocer et al.*, 2009a] and velocities [*Glocer et al.*, 2009b]. RAM-SCB has shown the ability to reproduce the global *Dst* index [*Rastätter et al.*, 2013], large-scale pressure distributions [*Jordanova et al.*, 2010b], and in situ magnetic field and fluxes [*Zaharia et al.*, 2010; *Yu et al.*, 2012; *Jordanova et al.*, 2014; *Yu et al.*, 2014].

These models are used to simulate the 31 August 2005 coronal mass ejection event. This is a moderate storm with a minimum observed *Dst* value of −131 nT, a maximum observed *Kp* value of 7, and an $F_{10.7}$ solar radio flux of 192×10^{-22} W/m^2/Hz. The solar wind drivers and associated interplanetary magnetic field (IMF) are shown in Figure 2. Notable of this storm are the more than seven continuous hours of southward oriented IMF, beginning just before 12 UT (Figure 2, third panel). This storm is simulated two ways: once with the RAM-SCB being fed inputs from the other models but with no pressure coupling (the one-way coupled case) and once with pressure feedback from RAM-SCB to BATS-R-US (the two-way coupled case). These two cases are compared so that the effect of the ring current on ionospheric outflow can be unambiguously investigated.
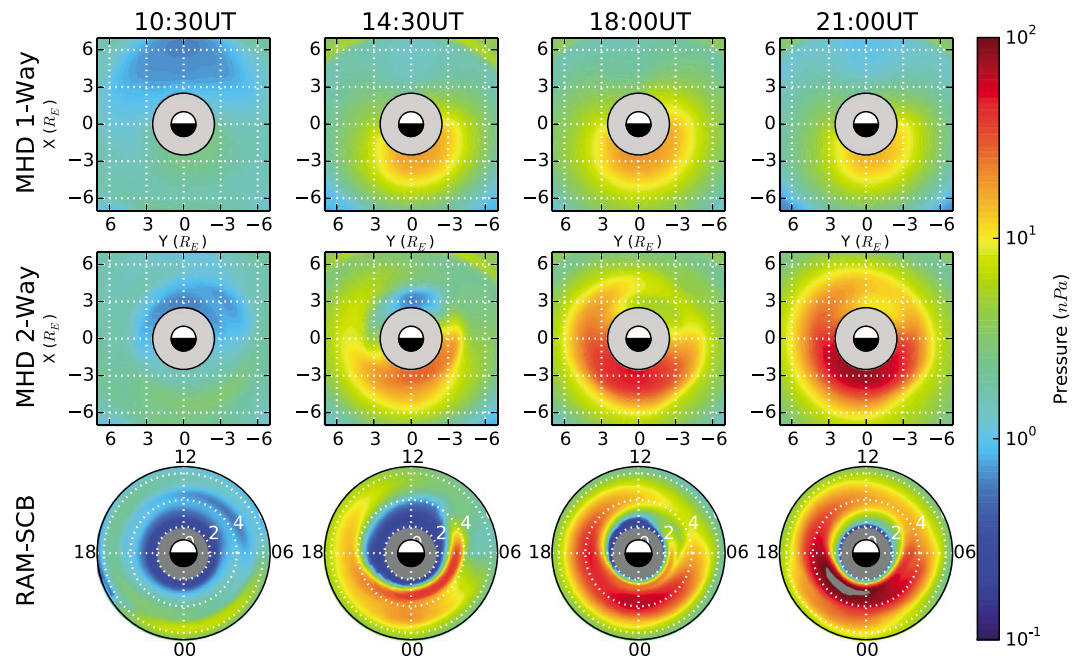
Figure 3. Equatorial pressure profiles from (top row) BATS-R-US without pressure coupling, (middle row) BATS-R-US with pressure coupling, and (bottom row) from RAM-SCB. Columns correspond to different epochs during the storm. All plots are arranged such that local noon is located at the top; all use the same color scale.

3. Results

3.1. Effects of Pressure Coupling on FACs

Figure 3 shows the equatorial pressure from BATS-R-US and RAM-SCB at four different times during the storm: prestorm, early storm, storm max, and early recovery (first to fourth columns, respectively). These epochs are marked by vertical dashed lines in Figure 2. Figure 3 (top row) shows the BATS-R-US pressure without two-way coupling; i.e., RAM-SCB is not returning its pressure to "nudge" the MHD pressure toward more realistic results. Without this coupling, the typical MHD behavior in the inner magnetosphere develops: a pressure increase that is weak (only a few tens of nPa at the peak) and relegated to a narrow magnetic local time (MLT) window about the nightside. In stark contrast is Figure 3 (bottom row), which shows the RAM-SCB results from the two-way coupled run at the same four epochs. The ring current pressure builds strongly and asymmetrically, reaching much higher values than its MHD counterpart (over 100 nPa) and begins to symmetrize toward the end of the storm. Figure 3 (middle row) shows the marriage of these two via two-way coupling between the models. While the MHD pressure patterns are slightly weaker and more diffuse than their bounce-averaged drift counterparts (owing to a coarser grid and the "nudging" approach), the RAM-SCB patterns are now clearly imposed onto the MHD solution. These results reflect what is expected of this coupling given previous, similar coupling efforts.

The increase in the inner magnetosphere pressure and, therefore, pressure gradients in the two-way coupled BATS-R-US simulations should result in stronger region 2 FACs, and Figure 4 shows just that. This figure is laid out similarly to Figure 3 in that each column corresponds to the same set of epochs along the storm; the first and second rows again correspond to one-way and two-way coupled model results. However, each frame now shows the radial currents passed from the MHD model to the ionospheric electrodynamics solver instead of equatorial pressure. In this picture, yellow contours are upward currents while blue values are downward currents. During prestorm (first column), neither simulation has had a chance to build up significant inner magnetosphere pressure. As such, the radial ionospheric currents appear near identical. As the storm progresses, however, differences emerge, especially at lower latitudes. The two-way coupled simulation has developed clear region 2 FACs; corresponding currents in the one-way coupled results are weaker, narrower in MLT extent, or simply nonexistent. The two-way coupled R1 FACs are also found at lower latitudes compared to the one-way results. Again, precedent for these results are well established.
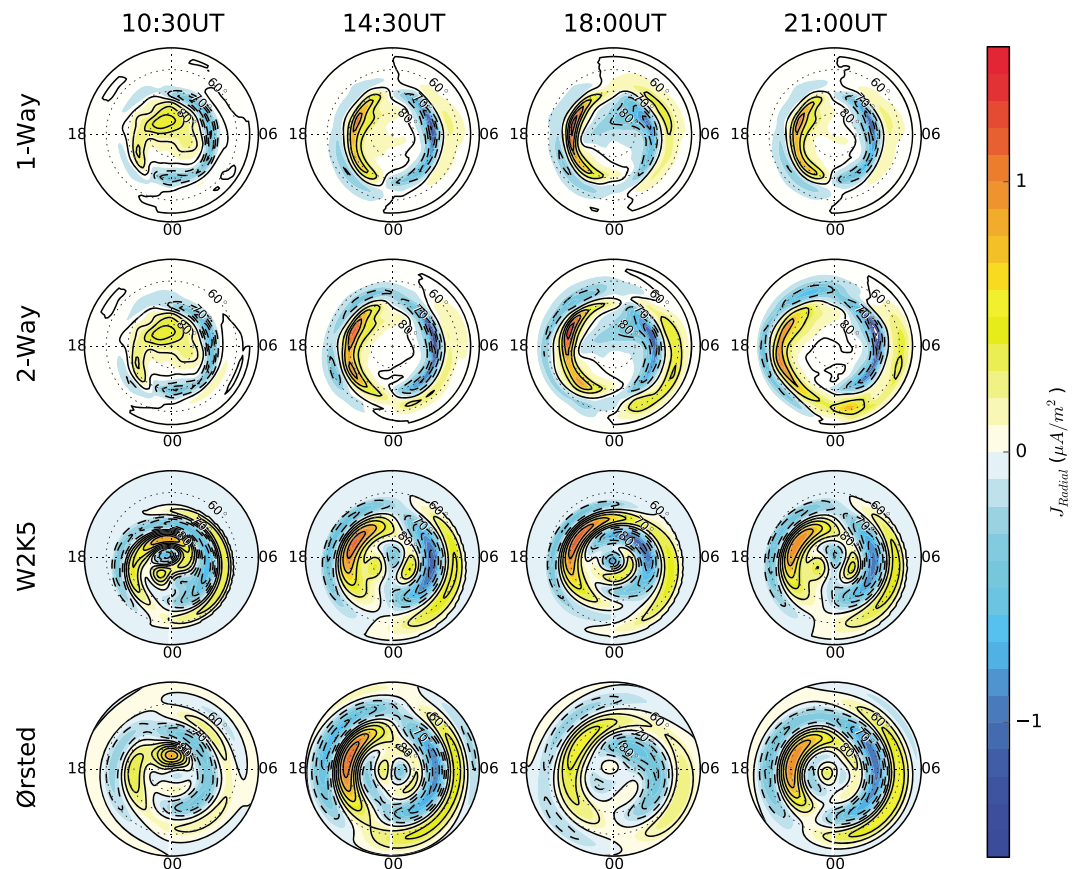
Figure 4. Field-aligned currents resulting from (first row) the one-way coupled simulation, (second row) the two-way coupled simulation, (third row) the W05 empirical model, and (fourth row) from fitting Ørsted-based magnetic field measurements. Each column corresponds to a different epoch from the storm.

To show that the two-way coupled results are more realistic than their one-way coupled counterparts, Figure 4 (third row) shows radial current density values obtained from the empirical model of *Weimer* [2005] (herein referred to as W05). This model was constructed from measurements with the Dynamics Explorer 2 (DE2) satellite, and it has two components: an electric potential model that is derived from the electric field measurements and a field-aligned current model that is derived from the magnetic field measurements. Magnetic potentials were derived from the magnetic field measurements, after subtraction of the International Geomagnetic Reference Field model, by an integration along the satellite orbit, using a method that is similar to the derivation of electric potentials from the electric field. The simultaneous solar wind velocity and IMF values are from the IMP 8 and ISEE 3 missions. The electric and magnetic potentials are based on spherical cap harmonic analysis (SCHA) [*Haines*, 1985] functions. A least error fit was used to obtain the SCHA coefficients as a function of the upstream solar wind drivers. The FAC values are obtained from the magnetic potentials by a two-dimensional Laplacian operation, as described in more detail by *Weimer* [2005]. The inputs for the W05 results presented in Figure 4 were ACE observations averaged over a 20 min window about the epochs shown in Figure 2. The W05 model and its predecessors have a long history of accurate predictions of ionospheric electrodynamics.

The comparison between the first-principles-based simulations (Figure 4, first and second rows) and the W05 model shows that the two-way coupled simulation more accurately captures the R2 FAC system than the one-way coupled simulation. Early in the simulation (first column), this is not evident, as neither RAM-SCB nor BATS-R-US has built up appreciable thermal pressure (Figure 3). This begins to change early in the storm (14:30 UT, second column), where the pressure coupling from RAM-SCB to BATS-R-US begins to drive stronger R2 FACs. Though weaker than the W05 prediction, the R2 FACs in the two-way coupled model case closely resemble its W05 counterpart in terms of local time extent, latitudinal extent, and position of peak current. As the storm progresses (18 and 21 UT, third and fourth columns, respectively), the agreement is even more

evident. Both the two-way coupled run and the W05 results show peak R2 upward current in the predawn sector and peak downward current in the postnoon sector. Again, the spatial extents of the currents are very similar. None of these similarities are shared with the one-way coupled run, which displays weak R2 FACs and disparate peak current positions. Clearly, the pressure coupling between RAM-SCB and BATS-R-US has improved this comparison.

To further demonstrate the validity of the two-way over the one-way coupled results, Figure 4 (fourth row) shows FAC values obtained in a different manner. The source data are from a magnetometer on the Ørsted satellite [*Olsen et al.*, 2000], from the years 1999 to 2005, and IMF measurements from ACE. The time span and volume of these data are much greater than what was available from DE2. FACs that are derived from the Ørsted data are shown in Figure 4 (fourth row). Rather than derived from an empirical model, magnetometer measurements were selected from time periods having IMF and dipole tilt values very similar to those at the times of the four specified epochs. SCHA coefficients for the magnetic potentials were fit directly from these binned magnetic field measurements. The FACs from the Ørsted observations support the conclusions drawn from the comparison of the global coupled model results to the W05 empirical model: inclusion of the pressure coupling greatly improves the R2 FACs in the global model. In terms of spatial distribution of the currents, the Ørsted-derived FACs agree best with the two-way coupled MHD/RAM-SCB results as the R2 currents are centered about lower latitudes than the W05 model. The magnitudes of the currents closely resemble that of the W05 model excluding the 18 UT pattern, which yields weaker currents than the other three models shown. This comparison again shows that the pressure coupling between RAM-SCB and BATS-R-US produces more realistic ionospheric results.

3.2. Coupling Effects on Outflow

Gombosi and Nagy [1989] demonstrated the effects of field-aligned current transients on ion outflow along a single, stationary flux tube. Notably, upward flowing currents are carried by precipitating (i.e., downward traveling) electrons which compress and heat the electron fluid. Ambipolar electric field is directly proportional to the electron pressure gradient [*Schunk and Nagy*, 2000]; therefore, the increased electron pressure gradient increases the ambipolar electric field. This culminates in an increase in heavy ion outflow. *Glocer et al.* [2009b] witnessed this behavior on a global scale when coupling many advecting flux tubes in PWOM to field-aligned currents formed in BATS-R-US. Flux tubes advecting into regions of upward current responded with increased heavy ion outflow, leading to a global pattern of increased O^+ fluxes corresponding to regions of upward current. In both studies, H^+ responds only tepidly to the increase in ambipolar fields. Based on these past studies, it would be expected that the R2 FACs driven by the pressure coupling would in turn drive stronger O^+ outflow.

Figure 5 illustrates the H^+ (first and second rows) and O^+ (third and fourth rows) fluxes at the top of the PWOM domain ($\sim 2.5 R_E$) for both the one-way coupled (i.e., no pressure coupling) simulation (first and third rows) and the two-way coupled simulation (second and fourth rows). Because PWOM flux tubes are radial and do not curve with the dipole field geometry, latitudes shown correspond to the latitude of flux tube foot point at the lower boundary of the model. The columns show results at the same epochs as Figures 3 and 4. Each white plus symbol marks where a PWOM flux tube is located at the time the 2-D slice is constructed.

Figure 5 demonstrates that the dynamics found in the previous studies also manifest here. Early in the storm (first column), PWOM exhibits weak upflows, the bulk of which are located toward the most strongly sunlit portion of the hemisphere. These fluxes correspond to weak driving and weak FACs (Figure 4, first column). As the storm begins and progresses (second to fourth columns), fluxes intensify. In both the one-way and two-way coupled results, the strongest oxygen outflows correspond to the locations of the upward currents from Figure 4. Though many processes factor into the outflow, the effects of flux tubes advecting in and out of FACs are evident.

Also evident is the role of the pressure coupling in the two-way coupled simulation in increasing O^+ fluxes well beyond those of the one-way coupled simulation. Upward directed FACs in the two-way coupled run (Figure 4, second row) are centered around 60° magnetic latitude and stretch from premidnight to prenoon, peaking in the postmidnight sector. These directly correspond to nightside O^+ flux peaks found in the PWOM results (Figure 5, fourth row). Additionally, though both the one-way and two-way simulations show O^+ flux intensifications corresponding to upward region 1 FACs, the two-way coupled simulation fluxes far exceed those of the one-way coupled simulation. This is likely due to region 2 FACs yet again. As flux tubes from the two-way coupled run advect from low latitudes on the dayside to the pole and across to the nightside, they first encounter the strong downward oriented region 2 field-aligned currents not present in the one-way
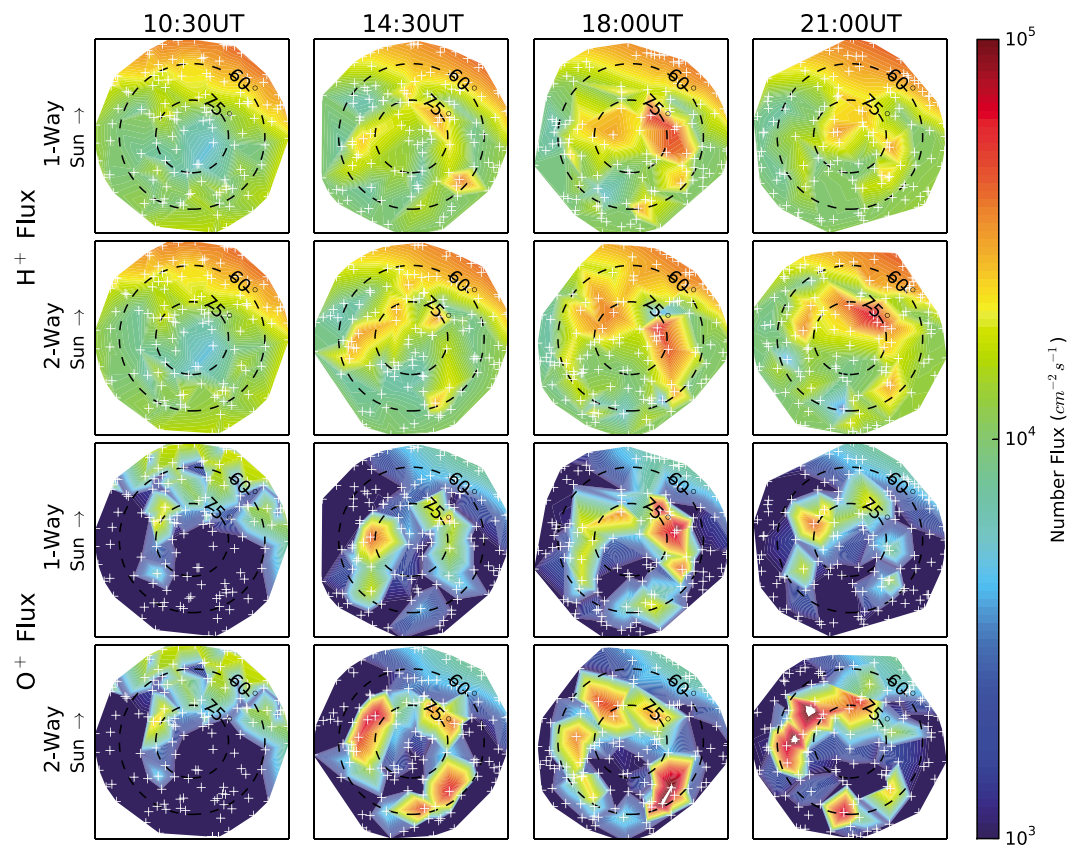
Figure 5. Upward fluxes from the PWOM with and without two-way coupling between RAM-SCB and BATS-R-US. Displayed are (first and second rows) H^+ (one way and two way) and (third and fourth rows) O^+. White plus signs indicate the instantaneous model flux tube locations. Each column corresponds to a different epoch during the storm.

coupled run. In these regions, electrons are flowing upward, expanding the electron fluid and lowering the electron pressure and the associated ambipolar field. As the flux tube advects into the upward directed region 1 FAC region, the increase in electron pressure is greater than if the flux tube had not first traveled through the downward current region, as is likely the case in the one-way coupled simulation. Thus, a greater O^+ outflow is generated compared to the case with weak or nonexistent region 2 FACs. As predicted by previous studies, H^+ fluxes are only slightly affected by these differences.

Figure 6 quantifies the differences in outflow by species. Total fluence, or flux integrated over the entire Northern Hemisphere, is plotted versus time over the duration of the simulation period. Fluences from the one-way coupled simulation are shown as solid lines, from the two-way coupled run as dashed lines. During the storm, total H^+ fluence (orange lines) is changed very little with the addition of pressure coupling between RAM-SCB and BATS-R-US. However, the total number of oxygen ions (green lines) entering the MHD domain is greatly increased with the addition of the pressure coupling, growing to a factor of 6 times that of the one-way coupled case. The net result is that the total contribution of plasma from the ionosphere to the magnetosphere (black lines) is doubled when the pressure coupling is activated.

3.3. Outflow Feedback to the Magnetosphere

The importance of heavy ion outflow on magnetospheric dynamics has been reinforced by recent studies that leverage observations, numerical models, or both. The pressure coupling between the ring current model and the global MHD model employed here has driven a dramatic increase in oxygen outflow. It is reasonable to expect an equally dramatic impact on magnetospheric dynamics.

The immediate effect of altering outflow patterns and magnitudes at gap region altitudes on the global system is illustrated by Figure 7. Each panel shows a noon-midnight meridian cut of BATS-R-US results with the Sun to the right. Magnetic field lines are shown in light grey; percent oxygen by number is shown as green contours. Two epochs are shown: early storm (14:30 UT, left column) and storm peak (18:00 UT, right column).
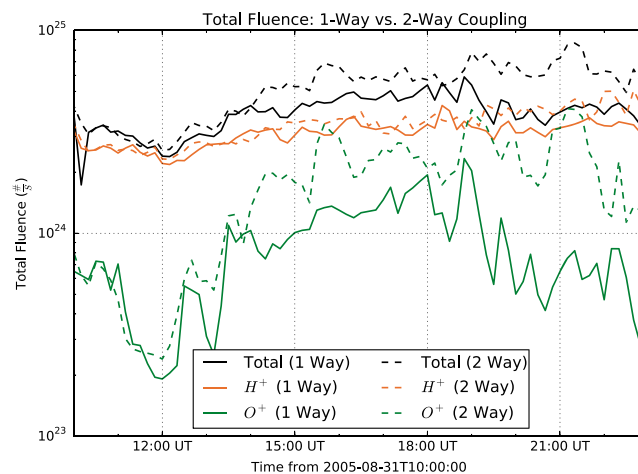
Figure 6. Hydrogen, oxygen, and total fluence (orange, green, and black lines, respectively) taken at the interface between the PWOM and BATS-R-US during the one-way coupled simulation (solid lines) and the two-way coupled simulation (dashed lines).

Figure 7 (top row) shows results from the one-way coupled simulation; Figure 7 (bottom row) shows results from the two-way coupled simulation. When the top and bottom rows are compared against each other, it becomes immediately obvious that the pressure coupling is driving an increase in oxygen entering the global magnetosphere system.

In each frame of Figure 7, two distinct oxygen outflow source regions are discernible near the inner boundary (grey circle) of the MHD domain: broad polar cap outflow, stemming from the region 1 FACs, and sharper, lower latitude jets stemming from region 2 FACs. Both of these sources become more oxygen rich as a direct result of the two-way coupling. Early in the storm event (Figure 7, left column), the one-way coupled simulation (top row) displays almost no midlatitude outflow; the oxygen originating from the polar region advects to the far tail and does not accumulate significantly within 10 R_E of the Earth. Conversely, the two-way coupled
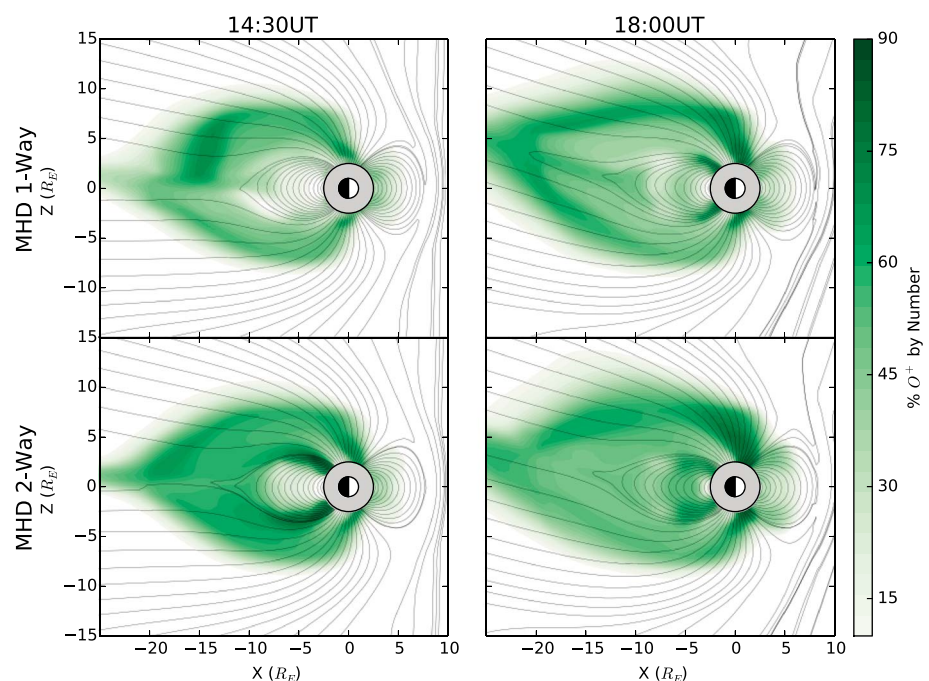

Figure 7. Noon-midnight meridian slices of BATS-R-US results in terms of percent oxygen by number (green contours) and magnetic field (gray lines) from the (top row) one-way coupled results and (bottom row) two-way coupled results. Each column corresponds to a separate storm epoch. The Sun is to the right.
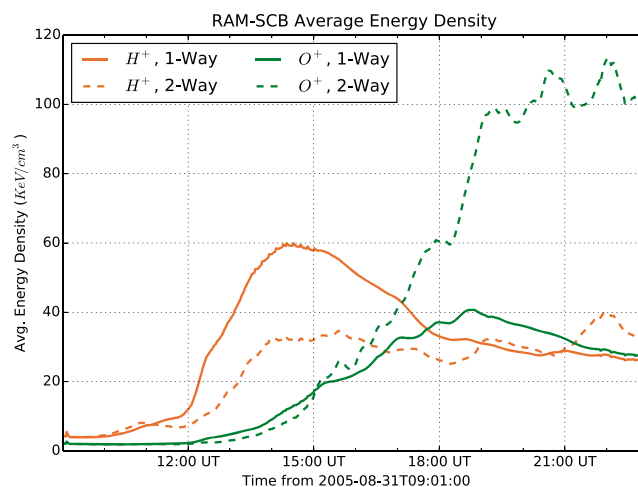
Figure 8. Average RAM-SCB oxygen (green) and hydrogen (orange) energy density for the one-way coupled (solid) and two-way coupled (dashed) simulations.

simulation shows significant midlatitude oxygen outflow, which mass loads the tail and begins to accumulate in the inner magnetosphere. During storm peak (Figure 7, right column), both simulations show an increase in oxygen from both sources. However, the area covered by the >60% contour in the two-way coupled simulation is much broader than that of the one-way simulation. The darker green contours indicate that more oxygen is present in the two-way coupled simulation in every region of interest: the lobes, tail and plasma sheet, and inner magnetosphere.

As the additional oxygen produced by the two-way coupling makes its way to the inner magnetosphere, it produces a ring current that is distinct from the one-way coupled ring current. This is quantified in Figure 8, which plots the average energy density per species in RAM-SCB versus time. In the one-way coupled simulation (solid lines), the onset of the storm brings a surge in hydrogen energy density (orange line). As this subsides, the average oxygen energy density (green line) slowly ramps up, briefly surpassing the hydrogen energy density just before 18 UT. At this point, both species contribute about equally to the average energy density of the ring current. In the two-way coupled simulation (dashed lines), the storm starts similarly but with a weaker initial hydrogen energy response. As the ring current builds up, the stronger region 2 FACs drive stronger oxygen outflow, and the average oxygen energy density in RAM-SCB sky rockets to more than twice that of the one-way coupled simulation. The ring current is now oxygen dominated instead of split evenly across the two major species.

The change in energy density due to the two-way coupling is evident in the resulting *Dst* indices calculated by the models, shown in Figure 9. The black dashed line shows the observed *Dst* index. The blue lines show *Dst* as calculated by BATS-R-US via a Biot-Savart integral, centered at $X = Y = Z = 0R_E$, of all electric currents within the MHD domain. Finally, the red lines show the *Dst* index as calculated by RAM-SCB via the Dessler-Parker-Sckopke relation [*Dessler and Parker*, 1959; *Sckopke*, 1966], including currents induced in the diamagnetic Earth. In the BATS-R-US results, the pressure coupling makes a dramatic difference. During the early storm phase, the two-way coupled *Dst* (blue dashed line) becomes strongly negative, a feature not observed in the one-way results (blue solid line). This is consistent with previous studies that demonstrate that without a two-way coupled inner magnetosphere model, ideal MHD is incapable of producing realistic *Dst* curves. During the storm peak and late main phases (after 18 UT), the effect of the additional oxygen outflow is evident as *Dst* plunges from ~ -50 to -144 nT, near the observed minimum of -122 nT over this period. A similar pattern is observed in the RAM-SCB results, though with less dramatic magnitudes. With only one-way coupling (solid red curve), the initial hydrogen injection drives a weak depression in the *Dst* (-37 nT minimum) that slowly recovers over the remainder of the simulated period. The two-way coupled RAM-SCB *Dst* reaches a minimum of -62 nT but only after the burst of oxygen energy density after 18 UT. In each case, the inclusion of the two-way coupling between RAM-SCB and BATS-R-US pushed the minimum *Dst* values toward the observed values. The timing of the MHD *Dst* strongly differs from the observed; potential reasons for this discrepancy are discussed below.
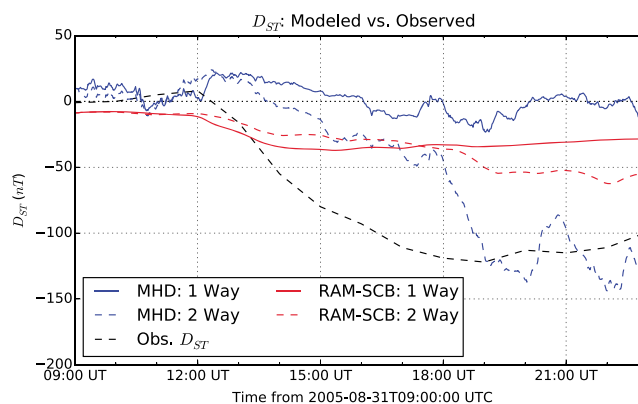
Figure 9. D_{ST} as calculated from BATS-R-US one-way and two-way coupled simulations (blue solid and dashed lines, respectively), RAM-SCB one-way and two-way coupled simulations (red solid and dashed lines), and observed values (black dashed line).

4. Conclusions and Discussion

This study leveraged two simulations to illustrate the relationship between the ring current and ionospheric outflow of heavy ions. The first simulation coupled outflow and the global magnetosphere to the ring current in a one-way manner; that is, no feedback from the ring current onto the rest of the system was allowed. The second simulation allowed this feedback via pressure coupling from the ring current to the global system. The addition of this two-way coupling ignited a cause-and-effect chain throughout the system: pressure gradients drove region 2 FACs, which amplified ionospheric ambipolar electric fields, which intensified escaping oxygen fluxes, which entered the plasma sheet and ring current and intensified the ring current. The net result is a ring current-outflow feedback loop that dramatically changed the storm time magnetosphere dynamics.

From these simulations, two clear conclusions can be drawn. First is that the ring current significantly contributes to the acceleration and outflow of ionospheric oxygen via region 2 field-aligned currents. Second, the additional oxygen outflow driven by ring current dynamics plays an important role in storm time magnetosphere and ring current development. Combining these two conclusions demonstrates a more fundamental observation: ionospheric outflow is not merely a source of plasma for the magnetosphere but a tightly integrated piece of the nonlinear magnetosphere-ionosphere system.

Though this study focuses on the effect of region 2 FACs on the results, other processes are affected by the two-way coupling as well. One example is the horizontal flow of the PWOM flux tubes as dictated by the ionospheric potential pattern. Speeding up the convection speed increases frictional heating of ions via low-altitude collisions with neutrals, while slowing the convection speed can change the amount of time flux tubes on the dayside remains sunlit. Both of these would have the effect of increasing the ions available to escape at higher latitudes by increasing the scale height of each species or increasing the low-altitude ion density, respectively. These processes do not appear to have a strong impact on these results. First, the cross polar cap potential curves from both simulations (not shown) are nearly identical, indicating similar convection speeds. Second, increased O^+ fluxes are primarily aligned with upward FACs (see Figure 5), as predicted by *Gombosi and Nagy* [1989]. For these reasons, the FAC effects on ambipolar electric field appear to be the most important driver of enhanced outflow.

This study also focuses on one aspect of FAC-driven outflow, i.e., the dynamic described by *Gombosi and Nagy* [1989]. However, FACs can drive additional outflow via other mechanisms. For example, precipitating electron flux produces enhanced ionization and increases electron temperature. Both factors can increase outflowing ion flux. In the current model setup, precipitation from the magnetosphere is assumed to be collocated with FACs and is passed to PWOM to drive these effects. The result appears to be secondary, however, as increased O^+ fluxes are primarily aligned with upward FACs, as stated above.

These conclusions harmonize with recent studies demonstrating a similar outflow-magnetosphere feedback loop that manifests in the tail during strong driving [*Brambles et al.*, 2011; *Ouellette et al.*, 2013]. The loop was set up by a large-scale dipolarization initiating a burst of transversely accelerated oxygen ions. The outflow then mass loads the plasma sheet, initializing another large-scale dipolarization, leading to the development

of sawteeth oscillations [e.g., *Henderson*, 2004]. The feedback loop investigated in this study differs in that it is established between the ring current and the ionosphere and can be set up during any period where substantial region 2 FACs develop.

The addition of the two-way coupling pushes the results toward observable reality, bolstering confidence in this study's conclusions. Foremost are the comparisons of the modeled FACs to the DE2 model and Ørsted data: the inclusion of the pressure coupling drives previously near-absent region 2 FACs to values and spatial distributions that closely match the empirically obtained values. Based on the work of *Cully et al.* [2003], the expected net particle fluences for this event ($F_{10.7}$ flux of 192 and maximum *Kp* of 7) are $\sim 10^{26}$ s^{-1} for O^+. The maximum O^+ fluence for the one-way coupled simulation over the storm period is 4.67×10^{24} s^{-1}, far below the expected values. Note that this number is obtained by multiplying the maximum Northern Hemisphere fluence value found in Figure 6 by 2. In the two-way coupled simulation, the maximum fluence increases to 8.23×10^{24} s^{-1}. H^+ fluences compare similarly: observed values at this activity level are expected to be $\sim 9 \times 10^{25}$ s^{-1}; two-way coupling increases the modeled H^+ fluence from 8.52×10^{24} s^{-1} to 1.01×10^{25} s^{-1}. While the modeled fluences for both species are still too low, the two-way coupling pushes the simulated values toward the observed values, especially for oxygen. The simulated *Dst* values follow a similar pattern: while the two-way coupling does not yield a perfect comparison, it does drive the results toward reality. The improvement is drastic for the BATS-R-US-calculated index, as the minimum value improves from a discrepancy of ~ 99 nT when compared to observed values to a difference of only ~ 22 nT. The improvement in *Dst* is related to a similar improvement in the expected ratio of oxygen to hydrogen energy density in the ring current. *Nosé* [2005], summarizing many independent studies, shows that this ratio is inversely proportional to *Dst*. As *Dst* drops below -100 nT, as is the case for the simulated event, the oxygen energy density surpasses that of hydrogen. In the simulations shown here, such a ratio is only obtained once the two-way coupling is activated. All of these comparisons show that the presence of the ring current-outflow feedback loop is driving the results toward reality.

Despite these improvements, there are still substantial differences between the observations and the model, especially concerning the amount of outflow. This discrepancy can be attributed to several factors. One possibility is insufficient topside electron heat flux, a value critical for setting the thermal electron temperature and, therefore, the ambipolar electric field. PWOM scales auroral and cusp heat fluxes against precipitating electron flux calculated between the MHD and ionosphere model; the scaling factor is the ratio of quiet time reference aurora heat flux to quiet time reference electron flux [*Welling et al.*, 2011]. If the reference values are not optimized to this event or if the precipitating electron flux is too low, the ambipolar electric field will suffer and outflow will be reduced. Another possibility is the necessity for additional acceleration mechanisms, such as wave-particle transverse heating effects [*Andre and Yau*, 1997; *Chaston et al.*, 2006], which is frequently observed to increase ion upflows [*Norqvist et al.*, 1998; *Sánchez and StrØmme*, 2014]. These issues require further investigation and potential improvements to the PWOM model but are not likely to diminish enhancement of oxygen outflows resulting from ring current-driven region 2 FACs.

There are likely many different factors driving the shortcomings of the *Dst* comparisons in Figure 9 as well. During the early storm (12–18 UT), modeled *Dst* values are only weakly depressed while the observed values drop quickly and reach near-minimum levels. During this period, the main pressure carrying species in the ring current is H^+ (Figure 8, orange lines). This initial hydrogen material can either be solar wind hydrogen that has mass loaded the tail prestorm [e.g., *Thomsen et al.*, 2003; *Welling and Ridley*, 2010a], ionospheric hydrogen excited by the storm onset, or ionospheric hydrogen that has mass loaded the lobe field lines prestorm [e.g., *Peterson et al.*, 2009]. A stronger ring current at the beginning of the storm is contingent on all three of these sources being captured properly by the coupled models. Though thorough investigation is required, a clue is provided via the lack of oxygen as an appreciable pressure carrier until 3 h after storm onset. This means that very little oxygen is in the lobes at storm onset. It may be that preconditioning of the magnetosphere-ionosphere-outflow system may be required to better capture early storm dynamics. However, this deficiency has little impact on the conclusions drawn concerning ring current-outflow interactions.

Despite these limitations, the results of this study strongly suggest that the ring current plays an important role in driving outflow of heavy ionospheric ions. For a moderate storm, this role can rival that of purely solar driving, implying that ring current feedback into outflow dynamics cannot be neglected in future modeling efforts. This is the second study, following *Brambles et al.* [2011], to demonstrate that leveraging causally

driven outflow can create nonlinear mass and energy feedback loops, further demonstrating the need to move toward a self-consistent, physics-based outflow implementation.

References

Anderson, B. J., S. -l. Ohtani, H. Korth, and A. Ukhorskiy (2005), Storm time dawn-dusk asymmetry of the large-scale Birkeland currents, *J. Geophys. Res.*, *110*, A12220, doi:10.1029/2005JA011246.

Andre, M., and A. Yau (1997), Theories and observations of ion energization and outflow in the high latitude magnetosphere, *Space Sci. Rev.*, *80*, 27–48.

Axford, W. I. (1968), The polar wind and the terrestrial helium budget, *J. Geophys. Res.*, *73*, 6855–6859, doi:10.1029/JA073i021p06855.

Banks, P. M., and T. E. Holzer (1968), The polar wind, *J. Geophys. Res.*, *73*, 6846–6854, doi:10.1029/JA073i021p06846.

Barakat, A. R., and R. W. Schunk (1983), O^+ ions in the polar wind, *J. Geophys. Res.*, *88*(A10), 7887, doi:10.1029/JA088iA10p07887.

Barakat, A. R., H. G. Demars, and R. W. Schunk (1998), Dynamic features of the polar wind in the presence of hot magnetospheric electrons, *J. Geophys. Res.*, *103*(A12), 29,289–29,304, doi:10.1029/98JA02827.

Brambles, O. J., W. Lotko, B. Zhang, M. Wiltberger, J. Lyon, and R. J. Strangeway (2011), Magnetosphere sawtooth oscillations induced by ionospheric outflow, *Science*, *332*(6034), 1183–1186, doi:10.1126/science.1202869.

Brambles, O. J., W. Lotko, B. Zhang, J. Ouellette, J. Lyon, and M. Wiltberger (2013), The effects of ionospheric outflow on ICME and SIR driven sawtooth events, *J. Geophys. Res. Space Physics*, *118*, 6026–6041, doi:10.1002/jgra.50522.

Buzulukova, N., M.-C. Fok, A. Pulkkinen, M. Kuznetsova, T. E. Moore, A. Glocer, P. C. Brandt, G. Tóth, and L. Rastätter (2010), Dynamics of ring current and electric fields in the inner magnetosphere during disturbed periods: CRCM-BATS-R-US coupled model, *J. Geophys. Res.*, *115*, A05210, doi:10.1029/2009JA014621.

Chappell, C. R., T. E. Moore, and J. H. Waite Jr. (1987), The ionosphere as a fully adequate source of plasma for the Earth's magnetosphere, *J. Geophys. Res.*, *92*, 5896–5910.

Chappell, C. R., B. L. Giles, T. E. Moore, D. C. Delcourt, P. D. Craven, and M. O. Chandler (2000), The adequacy of the ionospheric source in supplying magnetospheric plasma, *J. Atmos. Sol. Terr. Phys.*, *62*, 421–436.

Chaston, C. C., J. W. Bonnell, C. W. Carlson, J. P. McFadden, R. E. Ergun, R. J. Strangeway, and E. J. Lund (2004), Auroral ion acceleration in dispersive Alfvén waves, *J. Geophys. Res.*, *109*, A04205, doi:10.1029/2003JA010053.

Chaston, C. C., V. Genot, J. W. Bonnell, C. W. Carlson, J. P. McFadden, R. E. Ergun, R. J. Strangeway, E. J. Lund, and K. J. Hwang (2006), Ionospheric erosion by Alfvén waves, *J. Geophys. Res.*, *111*, A03206, doi:10.1029/2005JA011367.

Chaston, C. C., C. W. Carlson, J. P. McFadden, R. E. Ergun, and R. J. Strangeway (2007), How important are dispersive Alfvén waves for auroral particle acceleration?, *Geophys. Res. Lett.*, *34*, L07101, doi:10.1029/2006GL029144.

Cladis, J. B. (1986), Parallel acceleration and transport of ions from polar ionosphere to plasma sheet, *Geophys. Res. Lett.*, *13*, 893–896, doi:10.1029/GL013i009p00893.

Cully, C. M., E. Donovan, A. W. Yau, and G. G. Arkos (2003), Akebono/Suprathermal Mass Spectrometer observations of low-energy ion outflow: Dependence on magnetic activity and solar wind conditions, *J. Geophys. Res.*, *108*(A2), 1093, doi:10.1029/2001JA009200.

Daglis, I. A., R. M. Thorne, W. Baumjohann, and S. Orsini (1999), The terrestrial ring current: Origin, formation, and decay, *Rev. Geophys.*, *37*, 407–438, doi:10.1029/1999RG900009.

Delcourt, D. C., J. A. Sauvaud, and T. E. Moore (1993), Polar wind ion dynamics in the magnetotail, *J. Geophys. Res.*, *98*(A6), 9155–9169, doi:10.1029/93JA00301.

Denton, M. H., M. F. Thomsen, H. Korth, S. Lynch, J. C. Zhang, and M. W. Liemohn (2005), Bulk plasma properties at geosynchronous orbit, *J. Geophys. Res.*, *110*, A07223, doi:10.1029/2004JA010861.

Dessler, A. J., and E. N. Parker (1959), Hydromagnetic theory of geomagnetic storms, *J. Geophys. Res.*, *64*, 2239–2252.

De Zeeuw, D., S. Sazykin, R. Wolf, T. Gombosi, A. Ridley, and G. Tóth (2004), Coupling of a global MHD code and an inner magnetosphere model: Initial results, *J. Geophys. Res.*, *109*, A12219, doi:10.1029/2003JA010366.

De Zeeuw, D. L., T. I. Gombosi, C. P. T. Groth, K. G. Powell, and Q. F. Stout (2000), An adaptive MHD method for global space weather simulations, *IEEE Trans. Plasma Sci.*, *28*, 1956–1965.

Ebihara, Y., and M. Ejiri (2000), Simulation study on fundamental properties of the storm-time ring current, *J. Geophys. Res.*, *105*, 15,843–15,859.

Elliott, H. A., R. H. Comfort, P. D. Craven, M. O. Chandler, and T. E. Moore (2001), Solar wind influence on the oxygen content of ion outflow in the high-altitude polar cap during solar minimum conditions, *J. Geophys. Res.*, *106*(A4), 6067–6084, doi:10.1029/2000JA003022.

Fang, X., M. W. Liemohn, J. U. Kozyra, D. S. Evans, A. D. DeJong, and B. A. Emery (2007a), Global 30–240 keV proton precipitation in the 17–18 April 2002 geomagnetic storms: 1. Patterns, *J. Geophys. Res.*, *112*, A05301, doi:10.1029/2006JA011867.

Fang, X., M. W. Liemohn, J. U. Kozyra, and D. S. Evans (2007b), Global 30–240 keV proton precipitation in the 17–18 April 2002 geomagnetic storms: 2. Conductances and beam spreading, *J. Geophys. Res.*, *112*, A05302, doi:10.1029/2006JA012113.

Fang, X., A. J. Ridley, M. W. Liemohn, J. U. Kozyra, and D. S. Evans (2007c), Global 30–240 keV proton precipitation in the 17–18 April 2002 geomagnetic storms: 3. Impact on the ionosphere and thermosphere, *J. Geophys. Res.*, *112*, A07310, doi:10.1029/2006JA012144.

Fok, M., T. E. Moore, J. U. Kozyra, G. C. Ho, and D. C. Hamilton (1995), Three-dimensional ring current decay model, *J. Geophys. Res.*, *100*, 9619–9632.

Fok, M.-C., T. E. Moore, S. P. Slinker, J. A. Fedder, D. C. Delcourt, M. Nosé, and S.-H. Chen (2011), Modeling the superstorm in November 2003, *J. Geophys. Res.*, *116*, A00J17, doi:10.1029/2010JA015720.

Frey, H. U. (2004), Subauroral morning proton spots (SAMPS) as a result of plasmapause-ring-current interaction, *J. Geophys. Res.*, *109*, A10305, doi:10.1029/2004JA010516.

Galand, M., and A. D. Richmond (2001), Ionospheric electrical conductances produced by auroral proton precipitation, *J. Geophys. Res.*, *106*(A1), 117–125, doi:10.1029/1999JA002001.

Ganguli, S. B. (1996), The polar wind, *Rev. Geophys.*, *34*, 311–348, doi:10.1029/96RG00497.

Glocer, A., T. Gombosi, G. Toth, K. Hansen, A. Ridley, and A. Nagy (2007), Polar wind outflow model: Saturn results, *J. Geophys. Res.*, A01304, doi:10.1029/2006JA011755.

Glocer, A., G. Tóth, T. Gombosi, and D. T. Welling (2009a), Modeling ionospheric outflows and their impact on the magnetosphere, initial results, *J. Geophys. Res.*, *114*, A05216, doi:10.1029/2009JA014053.

Glocer, A., G. Tóth, T. Ma, Y. Gombosi, J. Zhang, and L. Kistler (2009b), Multi-fluid BATS-R-US: Magnetospheric composition and dynamics during geomagnetic storms, initial results, *J. Geophys. Res.*, *114*, A12203, doi:10.1029/2009JA014418.

Glocer, A., N. Kitamura, G. Toth, and T. Gombosi (2012), Modeling solar zenith angle effects on the polar wind, *J. Geophys. Res.*, *117*, A04318, doi:10.1029/2011JA017136.

Glocer, A., M. Fok, X. Meng, G. Toth, N. Buzulukova, S. Chen, and K. Lin (2013), CRCM + BATS-R-US two-way coupling, *J. Geophys. Res. Space Physics*, *118*, 1635–1650, doi:10.1002/jgra.50221.

Gombosi, T. I., and A. Nagy (1989), Time-dependent modeling of field-aligned current-generated ion transients in the polar wind, *J. Geophys. Res.*, *94*, 359–369.

Gombosi, T. I., D. L. De Zeeuw, C. P. T. Groth, K. G. Powell, and P. Song (1998), The length of the magnetotail for northward IMF: Results of 3D MHD simulations, in *Physics of Space Plasmas*, vol. 15, edited by T. Chang and J. R. Jasperse, pp. 121–128, MIT Press, Cambridge, Mass.

Haines, G. V. (1985), Spherical cap harmonic analysis, *J. Geophys. Res.*, *90*(B3), 2583–2591.

Hamilton, D. C., G. Gloeckler, F. M. Ipavich, W. Stüdemann, B. Wilken, and G. Kremser (1988), Ring current development during the great geomagnetic storm of February 1986, *J. Geophys. Res.*, *93*(A12), 14,343–14,355, doi:10.1029/JA093iA12p14343.

Henderson, M. G. (2004), The May 2–3, 1986 CDAW-9C interval: A sawtooth event, *Geophys. Res. Lett.*, *31*, L11804, doi:10.1029/2004GL019941.

Horwitz, J. L., C. W. Ho, H. D. Scarbro, G. R. Wilson, and T. E. Moore (1994), Centrifugal acceleration of the polar wind, *J. Geophys. Res.*, *99*(A8), 15,051–15,064, doi:10.1029/94JA00924.

Huddleston, M. M., C. R. Chappell, D. C. Delcourt, T. E. Moore, B. L. Giles, and M. O. Chandler (2005), An examination of the process and magnitude of ionospheric plasma supply to the magnetosphere, *J. Geophys. Res.*, *110*, A12202, doi:10.1029/2004JA010401.

Ilie, R., R. M. Skoug, P. Valek, H. O. Funsten, and A. Glocer (2013), Global view of inner magnetosphere composition during storm time, *J. Geophys. Res. Space Physics*, *118*, 7074–7084, doi:10.1002/2012JA018468.

Jordanova, V., L. Kistler, J. Kozyra, G. Khazanov, and A. Nagy (1996), Collisional losses of ring current ions, *J. Geophys. Res.*, *101*, 111–126.

Jordanova, V. K., J. U. Kozyra, A. F. Nagy, and G. V. Khazanov (1997), Kinetic model of the ring current-atmosphere interactions, *J. Geophys. Res.*, *102*, 14,279–14,291.

Jordanova, V. K., Y. S. Miyoshi, S. Zaharia, M. F. Thomsen, G. D. Reeves, D. S. Evans, C. G. Mouikis, and J. F. Fennell (2006), Kinetic simulations of ring current evolution during the Geospace Environment Modeling challenge events, *J. Geophys. Res.*, *111*, A11S10, doi:10.1029/2006JA011644.

Jordanova, V. K., J. Albert, and Y. Miyoshi (2008), Relativistic electron precipitation by EMIC waves from self-consistent global simulations, *J. Geophys. Res.*, *113*, A00A10, doi:10.1029/2008JA013239.

Jordanova, V. K., S. Zaharia, and D. T. Welling (2010a), Comparative study of ring current development using empirical, dipolar, and self-consistent magnetic field simulations, *J. Geophys. Res.*, *115*, A00J11, doi:10.1029/2010JA015671.

Jordanova, V. K., R. M. Thorne, W. Li, and Y. Miyoshi (2010b), Excitation of whistler mode chorus from global ring current simulations, *J. Geophys. Res.*, *115*, A00F10, doi:10.1029/2009JA014810.

Jordanova, V. K., Y. Yu, J. T. Niehof, R. M. Skoug, G. D. Reeves, C. A. Kletzing, J. F. Fennell, and H. E. Spence (2014), Simulations of inner magnetosphere dynamics with an expanded RAM-SCB model and comparisons with Van Allen Probes observations, *Geophys. Res. Lett.*, *41*, 2687–2694, doi:10.1002/2014GL059533.

Khazanov, G. V., M. W. Liemohn, and T. E. Moore (1997), Photoelectron effects on the self-consistent potential in the collisionless polar wind, *J. Geophys. Res.*, *102*(A4), 7509–7521, doi:10.1029/96JA03343.

Korth, H., L. Rastätter, B. J. Anderson, and A. J. Ridley (2011), Comparison of the observed dependence of large-scale Birkeland currents on solar wind parameters with that obtained from global simulations, *Ann. Geophys.*, *29*(10), 1809–1826, doi:10.5194/angeo-29-1809-2011.

Kozyra, J. U. (2002), Multistep *Dst* development and ring current composition changes during the 4–6 June 1991 magnetic storm, *J. Geophys. Res.*, *107*(A8), 1224, doi:10.1029/2001JA000023.

Kozyra, J. U., M.-C. Fok, E. R. Sanchez, D. S. Evans, D. C. Hamilton, and A. F. Nagy (1998), The role of precipitation losses in producing the rapid early recovery phase of the great magnetic storm of February 1986, *J. Geophys. Res.*, *103*(A4), 6801–6814.

Kronberg, E. A., S. E. Haaland, P. W. Daly, E. E. Grigorenko, L. M. Kistler, M. Fränz, and I. Dandouras (2012), Oxygen and hydrogen ion abundance in the near-Earth magnetosphere: Statistical results on the response to the geomagnetic and solar wind activity conditions, *J. Geophys. Res.*, *117*, A12208, doi:10.1029/2012JA018071.

Lennartsson, O. W., H. L. Collin, and W. K. Peterson (2004), Solar wind control of Earth's H^+ and O^+ outflow rates in the 15-eV to 33-keV energy range, *J. Geophys. Res.*, *109*, A12212, doi:10.1029/2004JA010690.

Lennartsson, W., and E. G. Shelley (1986), Survey of 0.1- to 16-keV/e plasma sheet ion composition, *J. Geophys. Res.*, *91*, 3061–3076.

Liemohn, M. W., J. U. Kozyra, V. K. Jordanova, G. V. Khazanov, M. F. Thomsen, and T. E. Cayton (1999), Analysis of early phase ring current recovery mechanisms during geomagnetic storms, *Geophys. Res. Lett.*, *26*, 2845–2848.

Liemohn, M. W., J. U. Kozyra, C. R. Clauer, and A. J. Ridley (2001), Computational analysis of the near-Earth magnetospheric current system during two-phase decay storms, *J. Geophys. Res.*, *106*, 29,531–29,542.

Ma, Y., A. F. Nagy, K. C. Hansen, D. L. De Zeeuw, T. I. Gombosi, and K. Powell (2002), Three-dimensional multispecies MHD studies of the solar wind interaction with Mars in the presence of crustal fields, *J. Geophys. Res.*, *107*(A10), 1282, doi:10.1029/2002JA009293.

Moore, T., M.-C. Fok, D. Delcourt, S. Slinker, and J. Fedder (2007), Global aspects of solar wind-ionosphere interactions, *J. Atmos. Sol. Terr. Phys.*, *69*(3), 265–278, doi:10.1016/j.jastp.2006.08.009.

Moore, T., M.-C. Fok, and K. Garcia-Sage (2014), The ionospheric outflow feedback loop, *J. Atmos. Sol. Terr. Phys.*, *115-116*, 59–66, doi:10.1016/j.jastp.2014.02.002.

Moore, T. E. (2005), Plasma sheet and (nonstorm) ring current formation from solar and polar wind sources, *J. Geophys. Res.*, *110*, A02210, doi:10.1029/2004JA010563.

Moore, T. E., and D. C. Delcourt (1995), The geopause, *Rev. Geophys.*, *33*, 175–210, doi:10.1029/95RG00872.

Moore, T. E., W. K. Peterson, C. T. Russell, M. O. Chandler, M. R. Collier, H. L. Collin, P. D. Craven, R. Fitzenreiter, B. L. Giles, and C. J. Pollock (1999), Ionospheric mass ejection in response to a CME, *Geophys. Res. Lett.*, *26*, 2339–2342.

Norqvist, P., M. André, and M. Tyrland (1998), A statistical study of ion energization mechanisms in the auroral region, *J. Geophys. Res.*, *103*(A10), 23,459–23,473, doi:10.1029/98JA02076.

Nosé, M. (2005), Overwhelming O^+ contribution to the plasma sheet energy density during the October 2003 superstorm: Geotail/EPIC and IMAGE/LENA observations, *J. Geophys. Res.*, *110*, A09S24, doi:10.1029/2004JA010930.

Nosé, M., R. W. McEntire, and S. P. Christon (2003), Change of the plasma sheet ion composition during magnetic storm development observed by the Geotail spacecraft, *J. Geophys. Res.*, *108*, 1201, doi:10.1029/2002JA009660.

Olsen, N., et al. (2000), Ørsted initial field model, *Geophys. Res. Lett.*, *27*(22), 3607–3610, doi:10.1029/2000GL011930.

Ouellette, J. E., O. J. Brambles, J. G. Lyon, W. Lotko, and B. N. Rogers (2013), Properties of outflow-driven sawtooth substorms, *J. Geophys. Res. Space Physics*, *118*(6), 3223–3232, doi:10.1002/jgra.50309.

Pembroke, A., F. Toffoletto, S. Sazykin, M. Wiltberger, J. Lyon, V. Merkin, and P. Schmitt (2012), Initial results from a dynamic coupled magnetosphere-ionosphere-ring current model, *J. Geophys. Res.*, *117*, A02211, doi:10.1029/2011JA016979.

Peterson, W., L. Andersson, B. Callahan, S. Elkington, R. Winglee, J. Scudder, and H. Collin (2009), Geomagnetic activity dependence of O^+ in transit from the ionosphere, *J. Atmos. Sol. Terr. Phys.*, *71*(16), 1623–1629, doi:10.1016/j.jastp.2008.11.003.

Powell, K., P. Roe, T. Linde, T. Gombosi, and D. L. De Zeeuw (1999), A solution-adaptive upwind scheme for ideal magnetohydrodynamics, *J. Comput. Phys.*, *154*, 284–309.

Pulkkinen, A., et al. (2013), Community-wide validation of geospace model ground magnetic field perturbation predictions to support model transition to operations, *Space Weather*, *11*(6), 369–385, doi:10.1002/swe.20056.

Rastätter, L., M. M. Kuznetsova, A. Vapirev, A. Ridley, M. Wiltberger, A. Pulkkinen, M. Hesse, and H. J. Singer (2011), Geospace environment modeling 2008–2009 challenge: Geosynchronous magnetic field, *Space Weather*, *9*, S04005, doi:10.1029/2010SW000617.

Rastätter, L., et al. (2013), Geospace environment modeling 2008–2009 challenge: Dst index, *Space Weather*, *11*, 187–205, doi:10.1002/swe.20036.

Ridley, A., T. Gombosi, and D. L. De Zeeuw (2004), Ionospheric control of the magnetospheric configuration: Conductance, *Ann. Geophys.*, *22*, 567–584.

Ridley, A. J., K. C. Hansen, G. Tóth, D. L. De Zeeuw, T. I. Gombosi, and K. G. Powell (2002), University of Michigan MHD results of the GGCM metrics challenge, *J. Geophys. Res.*, *107*(A10), 1290, doi:10.1029/2001JA000253.

Ridley, J. A., and M. W. Liemohn (2002), A model-derived storm time asymmetric ring current driven electric field description, *J. Geophys. Res.*, *107*(A8), 1151, doi:10.1029/2001JA000051.

Sánchez, E. R., and A. StrØmme (2014), Incoherent scatter radar-FAST satellite common volume observations of upflow-to-outflow conversion, *J. Geophys. Res. Space Physics*, *119*, 2649–2674, doi:10.1002/2013JA019096.

Sandanger, M., F. Søraas, K. Aarsnes, K. Oksavik, and D. S. Evans (2007), Loss of relativistic electrons: Evidence for pitch angle scattering by electromagnetic ion cyclotron waves excited by unstable ring current protons, *J. Geophys. Res.*, *112*, A12213, doi:10.1029/2006JA012138.

Schunk, R., and A. Nagy (2000), *Ionospheres: Physics, Plasma Physics, and Chemistry*, Cambridge Univ. Press, Cambridge, U. K.

Sckopke, N. (1966), A general relation between the energy of trapped particles and the disturbance field over the Earth, *J. Geophys. Res.*, *71*, 3125–3130.

Sharp, R. D., W. Lennartsson, and R. J. Strangeway (1985), The ionospheric contribution to the plasma environment in near-Earth space, *Radio Sci.*, *20*, 456–462, doi:10.1029/RS020i003p00456.

Siscoe, G. L., G. M. Erickson, B. U. O. Sonnerup, N. C. Maynard, K. D. Siebert, D. R. Weimer, and W. W. White (2001), Relation between cusp and mantle in MHD simulation, *J. Geophys. Res.*, *106*(A6), 10,743–10,749, doi:10.1029/2000JA000385.

Søraas, F., K. M. Laundal, and M. Usanova (2013), Coincident particle and optical observations of nightside subauroral proton precipitation, *J. Geophys. Res. Space Physics*, *118*, 1112–1122, doi:10.1002/jgra.50172.

Thomsen, M. F., J. E. Borovsky, R. M. Skoug, and C. W. Smith (2003), Delivery of cold, dense plasma sheet material into the near-Earth region, *J. Geophys. Res.*, *108*(A4), 1151, doi:10.1029/2002JA009544.

Tóth, G., et al. (2005), Space Weather Modeling Framework: A new tool for the space science community, *J. Geophys. Res.*, *110*, A12226, doi:10.1029/2005JA011126.

Tóth, G., D. L. D. Zeeuw, T. I. Gombosi, W. B. Manchester, A. J. Ridley, I. V. Sokolov, and I. I. Roussev (2007), Sun to thermosphere simulation of the October 28–30, 2003 storm with the Space Weather Modeling Framework, *Space Weather*, *5*, S06003, doi:10.1029/2006SW000272.

Tóth, G., et al. (2012), Adaptive numerical algorithms in space weather modeling, *J. Comput. Phys.*, *231*(3), 870–903, doi:10.1016/j.jcp.2011.02.006.

Tsyganenko, N. A. (1989), A magnetospheric magnetic field model with a warped tail current sheet, *Planet. Space Sci.*, *37*, 5–20.

Walker, R. J., M. Ashour-Abdalla, T. Ogino, V. Peroomian, and R. L. Richard (2003), Modeling magnetospheric sources, in *Earth's Low-Latitude Boundary Layer, Geophys. Monogr. Ser.*, vol. 133, edited by P. T. Newell and T. Onsager, pp. 33–43, AGU, Washington, D. C., doi:10.1029/133GM03.

Weimer, D. R. (2005), Predicting surface geomagnetic variations using ionospheric electrodynamic models, *J. Geophys. Res.*, *110*, A12307, doi:10.1029/2005JA011270.

Welling, D. T., and M. W. Liemohn (2014), Outflow in global magnetohydrodynamics as a function of a passive inner boundary source, *J. Geophys. Res. Space Physics*, *119*, 2691–2705, doi:10.1002/2013JA019374.

Welling, D. T., and A. J. Ridley (2010a), Exploring sources of magnetospheric plasma using multispecies MHD, *J. Geophys. Res.*, *115*, A04201, doi:10.1029/2009JA014596.

Welling, D. T., and A. J. Ridley (2010b), Validation of SWMF magnetic field and plasma, *Space Weather*, *8*, S03002, doi:10.1029/2009JA014596.

Welling, D. T., V. K. Jordanova, S. G. Zaharia, A. Glocer, and G. Toth (2011), The effects of dynamic ionospheric outflow on the ring current, *J. Geophys. Res.*, *116*, A00J19, doi:10.1029/2010JA015642.

Winglee, R. M. (1998), Multi-fluid simulations of the magnetosphere: The identification of the geopause and its variation with IMF, *Geophys. Res. Lett.*, *25*, 4441–4444.

Winglee, R. M. (2000), Mapping of ionospheric outflows into the magnetosphere for varying IMF conditions, *J. Atmos. Sol. Terr. Phys.*, *62*, 527–540.

Wolf, R. A. (1983), The quasi-static (slow-flow) region of the magnetosphere, in *Solar Terrestrial Physics*, edited by R. L. Carovillano and J. M. Forbes, pp. 303–368, D. Reidel Publishing, Hingham, Mass.

Yau, A. W., W. K. Peterson, and E. G. Shelley (1988), Quantitative parametrization of energetic ionospheric ion outflow, in *Modeling Magnetospheric Plasma, Geophys. Monogr. Ser.*, edited by T. E. Moore et al., pp. 211–217, AGU, Washington, D. C.

Young, D. T., H. Balsiger, and J. Geiss (1982), Correlations of magnetospheric ion composition with geomagnetic and solar activity, *J. Geophys. Res.*, *87*, 9077–9096.

Yu, Y., and A. J. Ridley (2008), Validation of the space weather modeling framework using ground-based magnetometers, *Space Weather*, *6*, S05002, doi:10.1029/2007SW000345.

Yu, Y., V. Jordanova, S. Zaharia, J. Koller, J. Zhang, and L. M. Kistler (2012), Validation study of the magnetically self-consistent inner magnetosphere model RAM-SCB, *J. Geophys. Res.*, *117*, A03222, doi:10.1029/2011JA017321.

Yu, Y., V. Jordanova, D. T. Welling, B. Larsen, S. G. Claudepierre, and C. Kletzing (2014), The role of ring current particle injections: Global simulations and Van Allen Probes observations during 17 March 2013 storm, *Geophys. Res. Lett.*, *41*, 1126–1132, doi:10.1002/2014GL059322.

Zaharia, S. (2008), Improved Euler potential method for three-dimensional magnetospheric equilibrium, *J. Geophys. Res.*, *113*, A08221, doi:10.1029/2008JA013325.

Zaharia, S., C. Cheng, and K. Maezawa (2004), 3-D force-balanced magnetospheric configurations, *Ann. Geophys.*, *22*, 251–265.

Zaharia, S., M. F. Thomsen, J. Birn, M. H. Denton, V. K. Jordanova, and C. Z. Cheng (2005), Effect of storm-time plasma pressure on the magnetic field in the inner magnetosphere, *Geophys. Res. Lett.*, *32*, L03102, doi:10.1029/2004GL021491.

Zaharia, S., V. K. Jordanova, M. F. Thomsen, and G. D. Reeves (2006), Self-consistent modeling of magnetic fields and plasmas in the inner magnetosphere: Application to a geomagnetic storm, *J. Geophys. Res.*, *111*, A11S14, doi:10.1029/2006JA011619.

Zaharia, S., V. K. Jordanova, D. T. Welling, and G. Tóth (2010), Self-consistent inner magnetosphere simulation driven by a global MHD model, *J. Geophys. Res.*, *115*, A12228, doi:10.1029/2010JA015915.

Zhang, J., et al. (2007), Understanding storm-time ring current development through data-model comparisons of a moderate storm, *J. Geophys. Res.*, *112*, A04208, doi:10.1029/2006JA011846.

Zheng, Y., A. T. Y. Lui, M.-C. Fok, B. J. Anderson, P. C. Brandt, T. J. Immel, and D. G. Mitchell (2006), Relationship between Region 2 field-aligned current and the ring current: Model results, *J. Geophys. Res.*, *111*, A11S06, doi:10.1029/2006JA011603.